



# Deformation mechanisms in ferritic/martensitic steels and the impact on mechanical design

Nasr M. Ghoniem\*, Giacomo Po, Shahram Sharafat

Mechanical & Aerospace Engineering, University of California, Los Angeles, Los Angeles, CA 90095, United States

## ARTICLE INFO

### Article history:

Available online 29 March 2013

## ABSTRACT

Structural steels for nuclear applications have undergone rapid development during the past few decades, thanks to a combination of trial-and-error, mechanism-based optimization, and multiscale modeling approaches. Deformation mechanisms are shown to be intimately related to mechanical design via dominant plastic deformation modes. Because mechanical design rules are mostly based on failure modes associated with plastic strain damage accumulation, we present here the fundamental deformation mechanisms for Ferritic/Martensitic (F/M) steels, and delineate their operational range of temperature and stress. The connection between deformation mechanisms, failure modes, and mechanical design is shown through application of design rules. A specific example is given for the alloy F82H utilized in the design of a Test Blanket Module (TBM) in the International Thermonuclear Experimental Reactor (ITER), where several constitutive equations are developed for design-related mechanical properties.

© 2013 Elsevier B.V. All rights reserved.

## 1. Introduction

F/M steels are under intensive world-wide development for applications in the nuclear industry. Structural applications encompass pressure vessels in Light Water Reactors (LWRs), cladding and core structure materials in Gen-IV fission systems, advanced pressure vessels in high-temperature Gen-IV reactors, as well as in structural materials for the First Wall/Blanket (FW/B) of Magnetic confinement Fusion Energy (MFE) reactors, and in the chamber of Inertial Confinement Fusion (IFE) systems. The performance and reliability of F/M steels in such diverse structural applications requires an understanding of their mechanical properties and deformation mechanisms under external loads, high heat flux, and neutron irradiation. Although the properties of F/M alloys are controlled by their specific composition and microstructure, some generic characteristics can be understood when one investigates various databases.

Mechanisms that lead to failure of F/M structural components in a nuclear environment are dependent on a number of variables, which can be grouped into two main categories: (1) *operational variables*, such as mechanical load, temperature, cycling, transients, and coolant type and (2) *material variables*, such as the composition and microstructure (dislocation density, grain size, lath boundaries, precipitates, solution hardening elements, etc.). The thrust of alloy and material optimization efforts is to control material variables so as to meet the demands imposed by operational variables.

Development of F/M steels has relied mostly on empirical, but sometimes on mechanistic procedures, in order to optimize steel compositions and processing methods for desired microstructure, which are known to engender excellent mechanical properties. The general methodology for the optimization of steel properties has been based on finding correlations between material processing techniques and the microstructure on the one hand, and the microstructure and the mechanical properties on the other. An illustration of the progress made on the improvement of the creep strength of F/M alloys is shown in Fig. 1, where the creep rupture strength is shown for various steel generations [1,2].

The driving force behind optimization of Gen-III and Gen-IV steels has been the long-term creep strength for service lifetimes greater than  $10^5$  h. One of the areas of concern here is the coarsening of carbide formers, such as  $M_{23}C_6$  and  $M_x$  type carbides after many years of service under stress conditions. The creep rupture strength when plotted versus service time shows a “sigmoidal” behavior, tending to a lower level of strength beyond  $10^4$ – $10^5$  h. Such behavior is attributed to the equilibrium concentration of elements like W, Mo and V in precipitates and in the matrix, giving rise to “solution hardening” as the eventual controlling mechanism of steels operating at long service lives. Thus, steel optimization efforts focused on the long-term stability of carbides in these systems. The fact that the service lifetime of the steel in the FW/B in fusion energy systems is expected to survive only a few years has led to a different development path regarding the long-term stability of carbide precipitates as compared to Gen-III and Gen-IV steels, developed for fission reactors.

Although development of specific grades of F/M steels for fusion energy applications followed a parallel path to the larger effort of

\* Corresponding author.

E-mail address: [ghoniem@seas.ucla.edu](mailto:ghoniem@seas.ucla.edu) (N.M. Ghoniem).

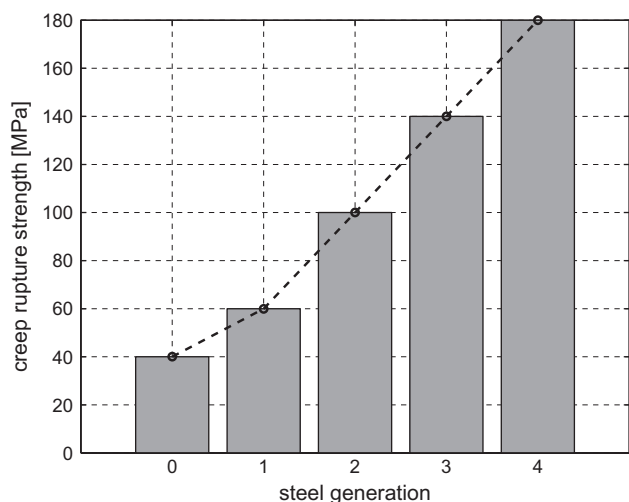


**Fig. 1.** The  $10^5$  h creep rupture strength (at 600 °C) of consecutive generations of steel for power plant applications [1].

their development for the power industry, we mention here two fundamental differences. First, early efforts in introducing generations of fusion steels have recognized the importance and possibility of developing steels that have the characteristic of being “low activation” [3]. Second, the expected lifetime of structural materials in FW/B applications is only a few years, as opposed to the 40–60 year target for steels employed in most power industries. The first constraint has led to the elimination of Mo, Nb, Ni, Cu and N, and the introduction of W and V as carbide formers in place of Mo, while Ta was introduced as a replacement for Nb. In addition, the 7–9% Cr range was found to be very suitable in elimination of the  $\delta$ -ferrite phase, which causes a reduction in fracture toughness.

Following parallel lines of development to fission reactor steels, the following generations of “fusion steels” have been developed (all compositions are in wt.%):

1. *Gen-I. Low Activation F/M Steels (LAFMs)*: The first low-activation steel was developed in the mid eighties on the basis of radioactivity and decay chain analysis of the main elements, and substitutions of Mo in low-Cr steels with V and W. The first such steel is the vanadium steel UCVS-1, with composition: 0.11C, 0.3Mn, 0.3Si, 2.46Cr, 0.05Ni, 1.5V, 0.02Mo, 0.007P, 0.015S, 0.015N, 0.043Al, 0.003Ti, 0.04Cu [4].
2. *Gen-II. Reduced Activation F/M Steels (RAFs)*: These steels have the composition range:  $\sim 0.1$ C, 0.04–0.3Si,  $\sim 0.45$ Mn, 8–9.4Cr, 1–2W,  $\sim 0.25$ V, 0.04–0.08Ta, 0.01–0.03N, 0.003–0.006B. They have been developed as follows:
  - (a) Japan: F82H, JLF-1.
  - (b) Europe: Eurofer, Optifer-I, Optifer-II.
  - (c) US: 9Cr-2WVTa.
3. *Gen-III. Oxide Dispersion Strengthened Reduced Activation F/M Steels (ODS-RAFM)*. These steels contain dispersoids of oxide particles (yttrium oxide and titanium oxide). Examples of steels under development are: PM2000, MA957, experimental grades of 9–12% Cr (martensites) and 12–20% Cr (ferrites). Although these steels are developed for fusion, they are also being considered for Gen-IV fission reactor steel applications in the cladding and structural supports. The alloy MA957 has a nominal composition 13.87Cr, 1.05Ti, 0.30Mo, 0.22Y<sub>2</sub>O<sub>3</sub>, 0.014C, 0.04Si, 0.13N, 0.1Al, 0.006S, while the alloy PM2000 has the composition of 19Cr, 5.5Al, 0.5Ti, 0.5Y<sub>2</sub>O<sub>3</sub>. W is sometimes used to replace Mo in fusion ODS steels, with lower Ti concentrations.

4. *Gen-IV. Super ODS-RAFM*. Mechanical alloying of metal and oxide powders is being developed to produce oxide dispersion-strengthened (ODS) ferritic alloys containing nano-scale oxide dispersoids. For example, the alloy 12YWT has the composition: 13.3Cr, 0.92W, 0.46Ti, 0.13Y, 0.19O. The stability of these dispersoids at high temperature and under irradiation has been studied recently. Ultrane Ti-, Y- and O-enriched particles were found to be extremely resistant to coarsening during isothermal aging at 1300 °C [5]. However, under heavy ion irradiations, nanoclusters were found to be unstable for high dose/dose-rate, and low temperature, while they were found to be stable at high dose/dose-rate, and high temperature. On the other hand, neutron irradiations in ATR up to 3 dpa, and at 500 °C contradict the results of ion irradiations, and thus further analysis is needed [6].

The objective of this paper is to investigate the deformation mechanisms of F/M steels on the basis of existing databases. Since failure modes are associated with the accumulation of plastic strain, we present the connection between operational and material variables through application of ASME and ITER design rules for mechanical components in a nuclear environment.

This paper is organized as follows. The basic mechanisms of deformation of F/M steels that lead to the accumulation of mechanical damage or the eventual failure by rupture or fracture are presented in Section 2, where we also discuss the main failure modes. Failure modes are primarily driven by the accumulation of plastic strain damage, and hence are largely determined by the rate of deformation (strain rate). The connection between mechanical design that attempts to meet the operational environment, and deformation mechanisms (determined by material properties) is made in Section 3. Finally, discussion and conclusions are given in Section 4.

## 2. Deformation mechanisms of F/M steels

Structural deformation beyond the elastic range results in permanent displacements within the material that creates dislocations, gaps, voids, and cracks as sites of material damage. The type and severity of each damage site is dependent on its specific location within the structure, and is thus difficult to pin point on a global scale. Mechanical design codes for inelastic structures are based on an acknowledgment of this fact; that damage accumulation is driven by plastic strain. It is thus prudent to set a global strain limit, since it is not possible to specify local strain limits at the level of the microstructure itself. Thus, there is a tacit assumption here that plastic deformation leads to failure. For example, both fatigue and creep limits are based on life fraction rules that measure damage in terms of fractions of accumulated strain to a maximum specified value. In this section, we first discuss the main failure modes of F/M steels in nuclear applications, and then focus on how these modes are driven by the rate of strain accumulation.

Development of structural components must consider possible failure modes of FW/B components. Thus, one must be cognizant of the connections between mechanical design and operation of FW/B components on the one hand, and material design for optimum performance on the other. Failure modes of FW/B components can be immediate at the start of operations, or delayed by prolonged damage accumulation due to thermal, stress and radiation effects on the microstructure. In developing and qualifying structural materials, one must therefore consider the following possible modes of failure:

1. Monotonic-type damage induced failure:
  - (a) Immediate plastic collapse.

- (b) Immediate plastic instability: either due to large deformation or to plastic flow localization.
- (c) Immediate fracture: either brittle or with exhaustion of ductility.
- (d) Thermal creep cavitation and rupture.
- 2. Cyclic-type damage induced failure.
  - (a) Progressive deformation (ratcheting).
  - (b) Progressive cracking (fatigue).
  - (c) Fatigue-creep type failure.
- 3. Irradiation accelerated and induced failure:
  - (a) Irradiation-induced immediate plastic instability due to flow localization.
  - (b) Irradiation-induced immediate fracture due to hardening, loss of ductility, and embrittlement due to helium and phase instabilities.
  - (c) Irradiation-accelerated thermal creep cavitation and rupture.
  - (d) Dimensional instabilities due to irradiation-induced creep and swelling.

We now discuss the deformation mechanisms and their relationship to material and operational variables, following the deformation map approach first proposed by Ashby [7], and then systematically adopted by Frost [8]. Similar fracture mechanisms maps have also been constructed by Zinkle and coworkers [9,10] for selected nuclear reactor materials. Deformation mechanism maps identify dominant deformation mechanisms by comparing their strain rates, which are modeled as functions of material and operational variables. In particular, we study the gen-II fusion grade F/M steel F82H and consider four types of deformation mechanisms and their relationship to two operational variables, namely the normalized tensile stress  $\sigma/\mu_0$  and homologous temperature  $T/T_m$  (where  $\mu_0$  is the shear modulus at 300 K and  $T_m$  is the melting temperature). In all our calculations we employ a piecewise<sup>1</sup> linear dependence of the shear modulus  $\mu$  on temperature, which was obtained fitting experimental data from [11]. Other material parameters for F82H are listed in Table 1. The four deformation mechanisms are:

1. *Crystal instability.* Crystals exhibit a theoretical shear strength corresponding to the shear stress required to shift planes of atoms with respect to neighboring planes in the absence of material defects. Above the theoretical shear strength, which can be taken as  $\mu/20$ , the crystal structure becomes unstable and immediate plastic collapse takes place. Therefore, the strain rate  $\dot{\epsilon}_1$  associated with crystal instability can be expressed as:

$$\dot{\epsilon}_1 = \begin{cases} \infty & \frac{\sigma}{\mu} \geq \frac{1}{20} \\ 0 & \frac{\sigma}{\mu} < \frac{1}{20} \end{cases} \quad (1)$$

2. *Plastic flow by dislocation glide.* The plastic strain rate due to dislocation glide is controlled by the flow stress  $\tau_f$ , which includes a contribution due to obstacles and, in body centered cubic (bcc) materials, a contribution arising from the lattice resistance. Since in heavily alloyed steels, such as F82H, the obstacle resistance is the dominant the rate-controlling mechanism, the strain rate for dislocation glide can be expressed as [7]:

$$\dot{\epsilon}_2 = \begin{cases} \dot{\epsilon}_0 \exp\left(-\frac{V(\tau_f - \sigma)}{kT}\right) & \sigma \geq \tau_0 \\ 0 & \sigma < \tau_0 \end{cases} \quad (2)$$

In Eq. (2),  $\dot{\epsilon}_0$  is a pre-exponential factor,  $V$  is the activation volume

**Table 1**

Material parameters for F82H in SI units. A distinction between the bcc phase ( $\alpha$  or  $\delta$  iron) and fcc phase ( $\gamma$  iron) is made when appropriate. Data from [7–9].

Description	$\alpha/\delta$	$\gamma$
$b$ Burgers vector (m)	$0.248 \times 10^{-9}$	$0.258 \times 10^{-9}$
$\Omega$ Atomic volume ( $\text{m}^3$ )	$1.18 \times 10^{-29}$	$1.21 \times 10^{-29}$
$A$ Dorn constant (–)	$7 \times 10^{13}$	$4.3 \times 10^5$
$n$ Power law creep exponent (–)	6.9	4.5
$D_{0v}$ Bulk diffusion coefficient ( $\text{m}^2/\text{s}$ )	$1 \times 10^{-4}$	$1 \times 10^{-5}$
$Q_{0v}$ Activation energy for bulk diffusion (J/mol)	$240 \times 10^3$	$270 \times 10^3$
$\dot{\epsilon}_0$ Prefactor for dislocation glide ( $\text{s}^{-1}$ )	$10^6$	–
$\mu_0$ Shear modulus at 300 K (Pa)	$84 \times 10^9$	–
$V$ Activation volume ( $\text{m}^3$ )	$100b^3$	–
$\tau_f$ Flow stress (Pa)	$320 \times 10^6$	–
$\tau_0$ Athermal part of $\tau_f$ (Pa)	$170 \times 10^6$	–
$d$ Average grain size (m)	$22 \times 10^{-6}$	–
$D_{0B}$ Grain boundary diff. coefficient ( $\text{m}^2/\text{s}$ )	$1 \times 10^{-4}$	–
$Q_{0B}$ Activation energy for g.b. diffusion (J/mol)	$150 \times 10^3$	–
$\delta$ G.b. cross section for diffusion transport (m)	$2b$	–

for dislocation glide and  $\tau_0$  is the athermal part of the flow stress.

3. *Diffusional creep:* At sufficiently high temperature, diffusion becomes the main mechanism of material transport. Following [7], we distinguish between two regimes, dominated by bulk diffusion (Nabarro–Herring creep, NH creep henceforth) and grain boundary diffusion (Coble creep), respectively. The strain rate for NH creep is given by:

$$\dot{\epsilon}_3 = 14 \frac{\sigma \Omega}{k_b T} \frac{1}{d^2} D_v \quad D_v = D_{0v} \exp\left(-\frac{Q_v}{RT}\right) \quad (3)$$

where  $\Omega$  is the atomic volume,  $d$  the average grain size and the bulk diffusion coefficient  $D_v$  depends on the pre-exponential factor  $D_{0v}$  and on the activation energy  $Q_{0v}$ . Similarly, for Coble creep we have:

$$\dot{\epsilon}_4 = 14 \frac{\sigma \Omega}{k_b T} \frac{1}{d^2} \frac{\pi \delta}{d} D_B \quad D_B = D_{0B} \exp\left(-\frac{Q_B}{RT}\right) \quad (4)$$

with  $\delta$  being the grain boundary cross section for diffusional transport. The overall strain rate due to diffusional creep is  $\dot{\epsilon}_3 + \dot{\epsilon}_4$ .

4. *Dislocation creep.* At high temperatures (typically defined as  $T > T_m/2$ ), the deformation mode is controlled by the formation and subsequent evolution of dislocation cell structures within each grain. The dislocation cell size is inversely proportional to the applied stress, and climb-controlled recovery of dislocations takes place within the cell walls. The rate of recovery is dictated by point defect diffusion, while the accumulation of plastic strain is governed by dislocation glide in between cell walls. Thus, it is expected that the deformation is diffusion controlled with a non-linear stress dependence as a result of dislocation glide. The appropriate constitutive equation is given by [12]:

$$\dot{\epsilon}_5 = A \frac{D_v \mu b}{kT} \left(\frac{\sigma}{\mu}\right)^n \quad (5)$$

where  $A$  and  $n$  are material parameters listed in Table 1.

The constitutive equations for strain rates are plotted in Fig. 2 as a function of normalized tensile stress and homologous temperature, in the range  $10^{-6} \leq \sigma/\mu_0 \leq 10^{-1}$  and  $0.05 \leq T/T_m \leq 1$ , respectively. Plastic strain rates lower than  $10^{-8} \text{ s}^{-1}$  are considered negligible and the corresponding area in the map is associated with elastic deformation. Fig. 3 illustrates what deformation mechanisms are encountered in power-plant components during

<sup>1</sup> A piecewise function was used to account for the change in the slope  $\frac{d\mu}{dT}$  corresponding to the martensite annealing temperature.



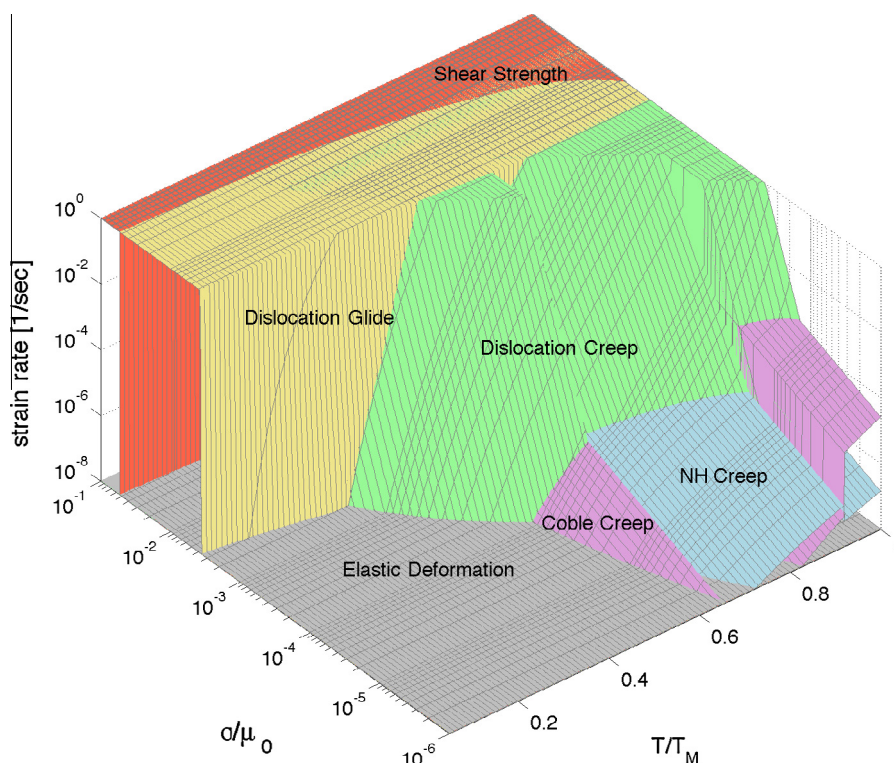


**Fig. 2.** Deformation mechanism map for F82H. Strain rates surfaces corresponding to the mechanisms described in Section 2 are plotted as a function of normalized tensile stress  $\sigma/\mu_0$  and homologous temperature  $T/T_M$ , in the range  $10^{-8} \leq \dot{\epsilon} \leq 10^0$  [s<sup>-1</sup>]. The highest strain rate determines the dominant deformation mechanism.

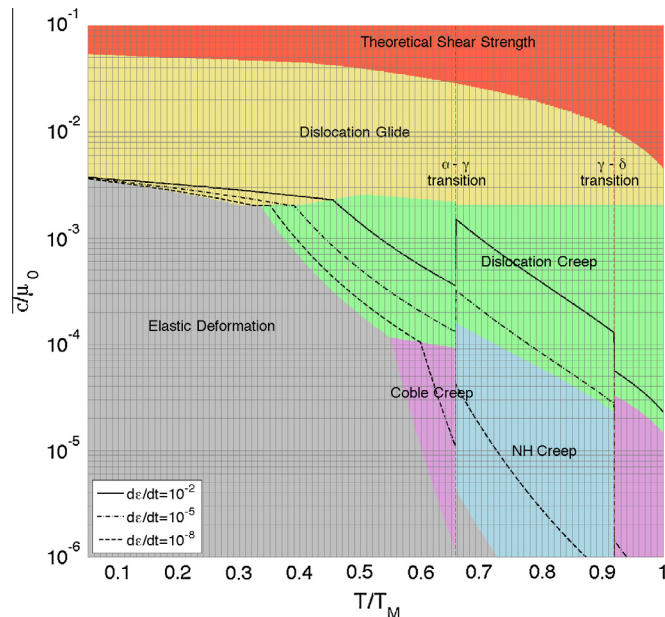


**Fig. 3.** Dominant deformation modes experienced by power plant components during different operational conditions: normal operations ( $\dot{\epsilon} \approx 10^{-8}$  s<sup>-1</sup>), startup/shutdown transient operations ( $\dot{\epsilon} \approx 10^{-5}$  s<sup>-1</sup>), off-normal conditions ( $\dot{\epsilon} \approx 10^{-2}$  s<sup>-1</sup>).

different typical operational conditions (associated with global strain rates).

### 3. Mechanical design criteria and corresponding property correlations for F82H

To assess the various deformation mechanisms of F/M steels and their relationship to failure modes, one must be cognizant of

the tight inter-relationship between criteria for mechanical design of nuclear components and key deformation mechanisms. Several design codes are used for qualification of high-temperature components in nuclear environments. The ASME Boiler & Pressure Vessel Code (ASME-BPV) is divided into 14 sections, the most relevant is Section III: Rules for Construction of Nuclear Power Plant Components. (ASME BPVC-III: rules for construction of nuclear power plant components – divisions 1 & 2 – subsections NB, NC, NCA, ND, NE, NF & NG – class 1, 2, & 3 components, and ASME BPVC-III NH: rules for construction of nuclear power plant components – division 1 – subsection NH – class 1 components in elevated temperature service) [13,14].

For fusion energy applications, structural design codes are still evolving. Presently, the code for Structural Design Criteria for In-Vessel Components (SDC-IC) contains interim rules for the structural design of the in-vessel components: first wall (FW), shield/blanket (B), divertor and the diagnostic components located inside of vacuum vessel for ITER. Future changes are expected for the construction of the DEMONstration Power Plant (DEMO). These criteria were developed because existing codes do not address the effects of irradiation on the in-vessel components. The component classifications used with existing codes for the construction of Nuclear Power Plants do not necessarily apply to the in-vessel components. The ITER Design Code Working Group began with the French code, RCC-MR, as a starting point and made modifications as necessary to account for the requirements of countries participating in the working group. The French RCC-MR Code (Design and Construction Rules for Mechanical Components of FBR Nuclear Island) has been issued by AFCEN (French Society for Design and Construction Rules for Nuclear Island Components). Since the ITER design code is based on both the ASME-BPV and RCC-MR French codes for design of nuclear components, we will first summarize the main criteria used to determine failure modes and structural reliability of nuclear components, in an effort to relate such criteria to deformation mechanisms [15,16].

### 3.1. Design criteria

To understand design criteria, we briefly discuss here the main definitions in the ITER design code:

1. **Primary stress:** primary stress is defined as that portion of the total stress which is required to satisfy equilibrium with the applied loading and which does not diminish after small scale permanent deformation.
2. **Secondary stress:** secondary stress is that portion of the total stress (minus peak stresses, as defined below), which can be relaxed as a result of small scale permanent deformation. The basic characteristic of a secondary stress is that it is self-limiting.
3. **Total stress (strain):** total stress  $\sigma_{ij}$  (strain  $\epsilon_{ij}$ ) is the stress (strain) under the effect of all the loadings to which the component is subjected.
4. **Membrane stress (strain):** membrane stress (or strain) tensor is the tensor whose components  $(\sigma_{ij})_m$  [ $(\epsilon_{ij})_m$ ] are equal to the mean value of stresses  $\sigma_{ij}(\epsilon_{ij})$  through the thickness.
5. **Bending stress (strain):** the bending stress (strain) tensor is that tensor whose components  $(\sigma_{ij})_b$  [ $(\epsilon_{ij})_b$ ] vary linearly through the thickness and which, when integrated through the thickness result in equilibrium with the section moment.
6. **Peak stress:** Peak stress is the increment of stress which is additive to the membrane- plus-bending stresses by reason of local discontinuities or local thermal stresses including the effects, if any, of stress concentrations.
7. **Stress intensity:** the stress intensity,  $\bar{\sigma}$ , at any given point is a scalar derived from the stress tensor,  $\sigma$ , at that point, using the maximum shear or Tresca criterion.
8. **Effective stress:** the effective stress used for creep calculation is based on von-Mises effective stress.
9. **Stress intensity range:** it is the maximum of the stress intensities of the tensor differences between the stress tensors  $\sigma(t)$  and  $\sigma(t)$  for every pair of times  $t$  and  $t$  within a cycle.
10. **Allowable primary membrane stress intensity ( $S_m$ ):**  $S_m$  is a temperature ( $T$ ) and fluence ( $\Phi t$ ) dependent allowable stress intensity defined as the least of the quantities:

$$S_m = \min \left[ \frac{1}{3} S_{u,min}(RT, 0), \frac{1}{3} S_{u,min}(T, 0), \frac{1}{3} S_{u,min}(T, \Phi t), \frac{2}{3} S_{y,min}(RT, 0), \frac{2}{3} S_{y,min}(T, 0), \frac{2}{3} S_{y,min}(T, \Phi t) \right] \quad (6)$$

where  $S_{y,min}$  and  $S_{u,min}$  are the minimum yield and ultimate tensile strengths, respectively, and  $RT$  is room temperature.

11. **Uniform elongation ( $\epsilon_u$ ):**  $\epsilon_u$  is defined as the plastic component of the engineering strain at the time when necking begins in a uniaxial tensile test.
12. **True strain at rupture ( $\epsilon_{tr}$ ):**  $\epsilon_{tr}$  is defined as:  $\ln \frac{100}{100-RA\%}$ , where  $RA$  is the reduction in area (%) as determined in a uniaxial tension test at a given temperature, strain rate, and fluence.
13. **Elastic follow-up factor ( $r$ ):** the  $r$ -factor provides a simplified inelastic analysis approach by which the peak inelastic strain and stress in a structure can be estimated from elastic analysis results. An  $r$  value equal to 4 is used in ISDC as a conservative estimate for many structures made of ductile alloys with adequate strain-hardening capability.
14. **Allowable primary plus secondary membrane stress intensity ( $S_e$ ):**  $S_e$  is a temperature ( $T$ ) and fluence ( $\Phi t$ ) dependent allowable stress intensity for a material with severe loss of uniform elongation due to irradiation and is defined as follows:

$$S_e = \begin{cases} \frac{1}{3} S_{u,min}(T, \Phi t) + \frac{E \epsilon_{tr}}{r_1} (\epsilon_u(T, \Phi t) - 0.02) & \text{if } \epsilon_u > 2\% \\ \frac{1}{3} S_{u,min}(T, \Phi t) & \text{if } \epsilon_u < 2\% \end{cases} \quad (7)$$

where  $E$  is Young's modulus,  $\alpha_1 = 0.5$ , and  $r_1 = \infty$  for  $\epsilon_u < 2\%$ , and  $r_1 = 4$  for  $\epsilon_u > 2\%$

15. **Allowable total stress intensity ( $S_d$ ):**  $S_d$  is a temperature ( $T$ ), fluence ( $\Phi t$ ), and  $r$ -factor dependent allowable stress intensity for total primary plus secondary stress in radiation embrittled materials, and is defined as follows:

$$S_d = \frac{2}{3} \left( S_{u,min}(T, \Phi t) + \frac{E \epsilon_{tr}(T, \Phi t)}{r \times TF} \right) \quad (8)$$

where  $TF$  = triaxiality factor to account for the effect of hydrostatic stress on ductility:  $TF = (\sigma_1 + \sigma_2 + \sigma_3)/\sigma_e$ , and  $r$  = elastic follow-up factor whose value is  $r_2$  in zones of stress concentration (i.e., peak stress due to stress concentration is included), and  $r_3$  away from zones of stress concentration.  $r_2 = \text{Max} \{K_T \& 4\}$  where  $K_T$  is the elastic stress concentration factor and  $r_3 = r_1$ .

16. **Time-dependent allowable primary stress intensity ( $S_t$ ):**  $S_t$  is a time and temperature-dependent allowable primary stress intensity defined as the least of the following: (1) two thirds of the minimum stress corresponding to average creep rupture time  $t$  at temperature  $T$ , (2) 80% of the minimum stress corresponding to time  $t$  and temperature  $T$  for onset of tertiary creep, and (3) minimum stress to cause a creep strain of  $\min[1\%, \epsilon_c/5]$  in time  $t$  and temperature  $T$ , where  $\epsilon_c$  is the minimum creep ductility.

The design rules are divided into a high temperature section and a low temperature section, depending on whether thermal creep effects are or are not important. The low temperature rules are always applicable. To determine whether the high temperature rules are also to be applied, the following negligible creep test should be used. Thermal creep is negligible over the total design lifetime of a component if the following summation limit is satisfied:

$$\sum_{i=1}^N \left( \frac{t_i}{t_{ci}} \right) \leq 1 \quad (9)$$

where the total lifetime is divided into  $N$  intervals of time; for each interval  $i$ , of duration  $t_i$ , the maximum allowable time at temperature is denoted by  $t_{ci}$ . The negligible thermal creep time  $t_{ci}$  at a temperature  $T_i$  is calculated as the time required to accumulate a thermal creep strain of 0.05% in a uniaxial creep specimen subjected to a constant stress of  $1.5 S_m(T_i)$ . If the inequality in Eq. 9 is satisfied, then only low temperature design rules need be applied. The following is a list of the design rules that must be met for components made of any structural material, and that we will apply to specific F/M alloys.

#### • Low-Temperature Design Rules:

1. **Necking and plastic instability limit:** To prevent failure by necking and plastic instability, the following limits must be satisfied at all times:

$$\overline{P_m} \leq S_m; \quad \overline{P_L + P_B} \leq K S_m(T_m, \Phi t_m). \quad (10)$$

where  $P_m$  is general primary membrane stress,  $P_L$  is local primary membrane stress,  $P_B$  is primary bending stress,  $K$  is bending shape factor (=1.5 for solid rectangular section), and  $S_m$  is evaluated at the thickness-averaged temperature ( $T_m$ ) and fluence ( $\Phi t_m$ )

2. **Plastic flow localization limit:** To prevent cracking due to plastic flow localization (in a material with significant loss of uniform elongation due to irradiation), the following limit must be satisfied at all times during the life of the component:

$$\overline{P_L + Q_L} \leq S_e(T_m, \Phi t_m). \quad (11)$$

3. **Ductility exhaustion limit:** To prevent local fracture due to exhaustion of ductility (due to embrittlement), the following limits must be satisfied at all times during the life of the component: The total stress, including peak stress, is limited by

$$\overline{P_L + P_b + Q + F} \leq S_d(T, \Phi t, r_2) \quad (12)$$

where  $F$  is peak stress (e.g., due to stress concentration), and the total stress, excluding peak stress, is limited by

$$\overline{P_L + P_b + Q} \leq S_d(T, \Phi t, r_3) \quad (13)$$

4. **Brittle fracture limit:** To prevent brittle fracture initiating from severe flaws or notches, the maximum mode I stress intensity factor,  $K_I$ , due to all primary and secondary loadings, including peak ( $P_L + P_b + Q + F$ ), must be limited by the following:

$$K_I \leq K_C(T_m, \Phi t) \quad (14)$$

where  $K_C$  is the linear-elastic fracture toughness evaluated at the thickness-averaged temperature and fluence. The stress intensity factor  $K_I$  has to be determined from the analysis of a postulated surface flaw of depth  $a_0$ , length  $4a_0$ , where  $a_0 = \max[4a_u, h/4]$ ,  $a_u$  = largest undetectable crack length, and  $h$  = section thickness. If the full section under consideration (without the flaw) experiences plasticity, a suitable non-linear fracture parameter (e.g., J-integral) should be used instead of  $K$ .

5. **Ratcheting limit:** To prevent ratcheting due to cyclic loading, either of the following two limits should be satisfied at all times:

- (a)  $3S_m$  limit:  $\overline{(P_L + P_b)}_{\max} + \Delta[\overline{P} + \overline{Q}]_{\max} \leq 3S_m(T_m, \Phi t_m)$  where  $\Delta$  denotes the range of primary ( $P$ ) and secondary ( $Q$ ) stress due to cyclic loading.

- (b) Bree-diagram limit:

$$Y \leq \begin{cases} \frac{1}{X} & \text{for } 0 \leq X \leq 0.5 \\ 4(1 - X) & \text{for } 0.5 < X \leq 1 \end{cases} \quad (15)$$

where  $X = \frac{\overline{P_m}}{S_y}$  or  $X = \frac{\overline{P_L + P_b}}{S_y}$  and  $Y = \frac{\Delta[\overline{P} + \overline{Q}]}{S_y}$

and the yield stress  $S_y$  is evaluated at the average of the thickness-averaged temperatures at the 'cold' and 'hot' ends of the cycle.

6. **Fatigue limit:** To prevent the initiation of a fatigue crack due to cyclic loading, the fatigue usage fraction  $V$  at the end of life must satisfy the following limit:

$$V = \sum_{j=1}^J \frac{n_j}{N_j(\Delta \varepsilon_j)} < 1 \quad (16)$$

where the lifetime is divided into  $J$  type of cycles. For each cycle type  $j$ , characterized by  $n_j$  cycles at an equivalent strain range  $\Delta \varepsilon_j$  and average temperature  $T_j$  during the cycle,  $N_j$  is the allowable cycles. If  $\Delta \varepsilon_j$  is calculated elastically, it should be corrected for possible plasticity effects (e.g., by Neubers rule for notches).

#### • High-Temperature Design Rules:

1. **Creep damage limit:** To guard against creep damage, the following limits must be satisfied:

$$\begin{aligned} \overline{P_m} &\leq S_t(T_m, t) \\ \overline{P_L + P_b/K_t} &\leq S_t(T_m, t) \end{aligned} \quad (17)$$

where  $t$  is the design lifetime, and  $K_t = (K + 1)/2$ . If the lifetime involves variable stress and temperature history, these equations should be replaced by limits on usage fraction sums.

2. **Creep-ratcheting limit:** If the negligible creep test is not satisfied, then in addition to satisfying the low temperature ratcheting limit based on Bree diagram, the high temperature ratcheting limit should be satisfied by first calculating an effective core stress  $\sigma_c$  for creep calculations as follows:

$$\sigma_c = Z S_{yL} \quad (18)$$

where  $S_{yL}$  is the  $S_y$  value at the 'low' temperature extreme of the cycle and  $Z$  is a creep stress parameter defined in terms of  $X$  and  $Y$ , as follows:

$$Z = \begin{cases} X & \text{for } X + Y \leq 1 \\ Y + 1 - 2\sqrt{(1 - X)Y} & \text{for } 1 - X \leq Y < \frac{1}{1 - X} \\ XY & \text{for } Y > \frac{1}{1 - X} \end{cases} \quad (19)$$

The total creep strain accumulated during the lifetime due to a stress  $1.25 \sigma_c$  should be less than  $\min[1\%, \varepsilon_C/5]$  where  $\varepsilon_C$  is the minimum creep ductility during the cycle. If the lifetime involves more than one types of cycles of stress and temperature, the criterion is satisfied by the use of usage fraction sums.

3. **Creep-fatigue limit:** If the negligible creep test is not satisfied, then creep damage ( $W$ ) has to be added to the fatigue damage ( $V$ ) evaluated as:

$$V + W < 1 \quad (20)$$

where  $W$  is the creep damage obtained by first dividing the lifetime into  $K$  intervals. Each interval  $k$  of duration  $t_k$  is characterized by a maximum temperature  $T_k$ , a maximum effective stress  $\sigma_{e,k}$ . The following sum defines the creep damage  $W$ :

$$W = \sum_{k=1}^K \frac{\Delta t_k}{t_{R,k}} \quad (21)$$

where  $t_{R,k}$  is the minimum time to creep rupture at temperature  $T_k$  and stress  $1.25 \sigma_{c,k}$ .

### 3.2. Design data for reduced activation martensitic steel F82H

The aim of this work is to present design-relevant data correlations of the F/M steel F82H data through analysis of the End Of Life (EOL) failure modes. The F/M steel F82H is selected as the mainline structural material for a potential U.S. ITER TBM, which has been estimated to accumulate a total neutron damage of 3.7 dpa. To this end, the design criteria outlined earlier here require correlations for average tensile yield strength ( $S_{y(av)}$ ), average ultimate tensile strength ( $S_{u(av)}$ ) as well as the irradiated counterparts,  $S_{y(irr)}$  and  $S_{u(irr)}$ . The average yield strengths and ultimate strength of F82H were reported by Tavassoli et al. [17]. However, at the time of publication, irradiated data were scarce and only a limited correlation for  $S_{y(irr)}$  was developed. In this section, we report on the development of correlations for the irradiated average yield and tensile strengths,  $S_{y(irr)}$  and  $S_{u(irr)}$ , based on more recent neutron irradiation data. Tavassoli et al. [17] published a database for F82H (IAE Heat) properties, and gave a correlation for  $S_{y(av)}$  as a function of temperature:

$$\begin{aligned} S_{y(av)}(T) = 558.76 - 0.81574T + 2.7621 \times 10^{-3}T^2 - 3.476 \\ \times 10^{-6}T^3 \end{aligned} \quad (22)$$

where  $T$  is temperature in Celsius and the strength is in MPa. In order to estimate the yield strength as a function of neutron damage (dpa), irradiation data of F82H IAE Heats 9741, 9753 [18], along with recent irradiation data of IAE Heat 974 [19,20] were reviewed and are plotted in Fig. 4.



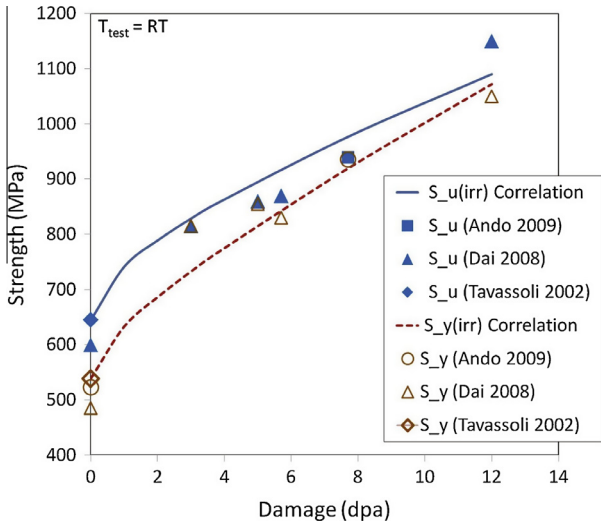


**Fig. 4.** Tensile yield and ultimate strengths for F82H as a function of displacement damage dose (HFIR:  $T_{irr} = 300$  °C; STIP-I:  $T_{irr} = 90$  °C to 375 °C – HFIR IEA Heat 9741, 9753; STIP-I: IEA Heat 974 [17]).

Based on the average yield strength (Eq. (22)), and the irradiation data [19,20], correlations for the average irradiated yield and ultimate strengths of F82H as a function of damage (dpa) and temperature have been developed. These are given by Eqs. (23) and (24), and shown in Fig. 4:

$$S_{y(irr)}(dpa, T) = S_{y(av,unirr)}(1 + 0.045 \times \Phi + 0.13\sqrt{\Phi}) \quad (23)$$

where  $\Phi$  is the accumulated displacement damage in dpa. The ultimate strength of F82H IEA Heat 9741 and 9753 was derived by [17] and is reproduced here by the following equation.

$$S_{u(av)} = 666.44 - 0.84514T + 2.1019 \times 10^{-3}T^2 - 2.617 \times 10^{-6}T^3 \quad (24)$$

Ando et al. [20] measured the room temperature (RT) irradiated Ultimate Tensile Strength (UTS) of F82H (IEA Heat 9741, 9753) at 7.7 dpa and  $T_{irr}$  of 300 °C. They showed a 51% increase in UTS (un-irradiated UTS 621.6 MPa; irradiated UTS<sub>irr</sub> 938.9 MPa; tested at RT). Furthermore, Dai et al. [19] reported results of irradiated ultimate tensile strength for F82H (IEA Heat 974) irradiated between 90 °C and 375 °C up to 12 dpa using spallation neutrons in the SINQ Target Irradiation Program (STIP-I). To correlate the effects of neutron damage on the UTS of F82H, we developed a simple equation similar to the correlation for irradiated yield strength (Eq. (23)):

$$S_{u(irr)}(dpa, T) = S_{u(av,unirr)}(1 + 0.02 \times \Phi + 0.13\sqrt{\Phi}) \quad (25)$$

Fig. 5 shows the irradiated ultimate tensile ( $S_{u(irr)}$ ) strength of F82H and the correlation for  $S_{u(irr)}$  (Eq. (25)), as a function of temperature at various displacement damage doses.

The correlations for the irradiated strength ( $S_{y(irr)}$  and  $S_{u(irr)}$ ) expressions can now be used to determine the allowable primary membrane stress intensity ( $S_m$ ), allowable primary plus secondary membrane stress intensity ( $S_e$ ), and the allowable total stress intensity ( $S_d$ ) as a function of temperature and neutron irradiation dose.

The low temperature design rules specify that the structure must avoid brittle fracture initiating from severe flaws and notches. The maximum mode-I stress intensity factor,  $K_I$ , due to all primary, secondary, and peak stress must be limited by the linear-elastic fracture toughness  $K_{IC}$ . To evaluate the structure's response to a postulated surface flaw following neutron damage, it is necessary to have correlations that relate  $K_{IC}$  to neutron

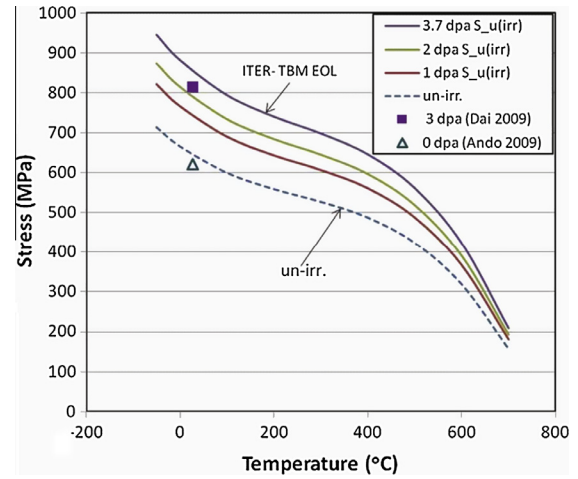


**Fig. 5.** Irradiated ultimate tensile ( $S_{u(irr)}$ ) strength of F82H (IEA Heats 9741, 9753) as a function of temperature based on correlations given by Eq. (25) (3 dpa at  $T_{irr} = 85$ –100 °C and 180 He-appm[19]).

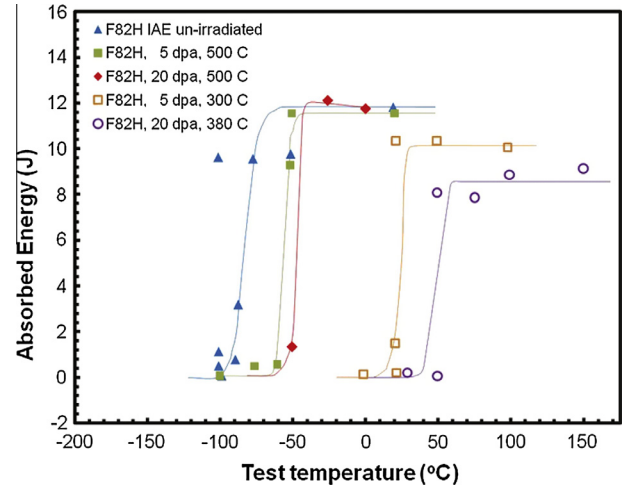


**Fig. 6.** Charpy V-Notch impact energy of F82H IEA Heat [23].

displacement damage ( $\Phi$ ) and corresponding irradiation temperature ( $T_{irr}$ ), the operating temperature ( $T$ ), the shift in ductile to brittle transition temperature (DBTT), and width of the transition temperature ( $T_{trans}$ ) region between the Lower Shelf Energy (LSE) and the Upper Shelf Energy (USE). We propose to represent the complex relationship of the fracture toughness on these variables by the following correlation for  $K_{IC(irr)}$ :

$$K_{IC(irr)} = K_0 + \frac{1}{2}[(K_{max}(1 - A(T_{irr})\Phi))] \times \left[ 1 + \tanh \left( \frac{T - T_0(1 + B(T_{irr})\Phi)}{\Delta T_{trans}} \right) \right] \quad (26)$$

where  $K_0$  corresponds to the lower shelf energy (LSE),  $K_{max}$  corresponds to the upper shelf energy (USE),  $A(T_{irr})$  is a coefficient to account for neutron damage effect on the USE,  $B(T_{irr})$  is a coefficient to account for neutron damage effect on the LSE,  $T$  is temperature,  $T_0$  the pre-irradiation DBTT,  $\Delta T_{trans}$  is a parameter that accounts for the transition region between LSE and USE, and  $\Phi$  is the neutron displacement damage dose in dpa. In order to obtain  $K_0$ ,  $K_{max}$ ,  $T_0$ , and  $\Delta T_{trans}$  parameters, the correlation is fitted to existing  $K_{IC}$  curves from the literature. The parameters  $A(T_{irr})$  and  $B(T_{irr})$  depend on the effect of damage on the LSE and USE, and therefore they were

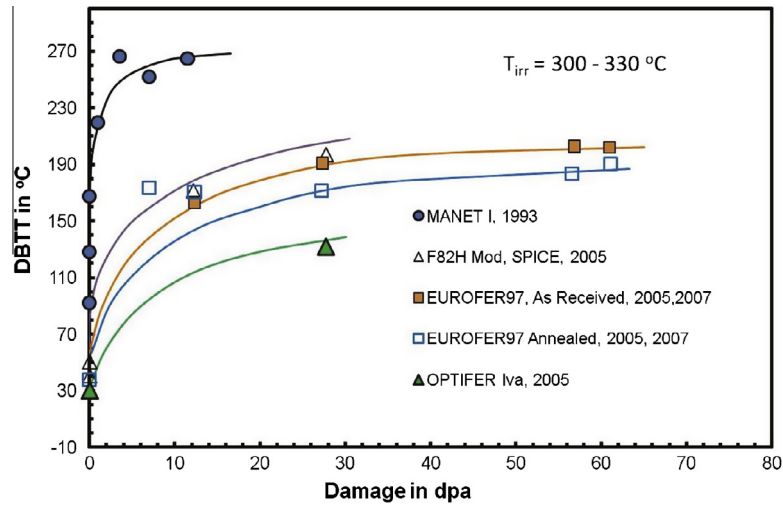


Fig. 7. Shift in the DBTT for a number of F/M steels as a function of neutron displacement damage dose [25,26].

correlated not only to published  $K_{IC}$  data but also to Charpy energy impact test data, for which there exists a larger database than for  $K_{IC(irr)}$  (see Figs. 6 and 7). A thorough analysis of the effects of helium and displacement damage on hardening and the shift in the DBTT is given by Yamamoto et al. [24].

The ITER TBM will experience a maximum damage of 3.7 dpa at irradiation temperatures between 350 °C and 560 °C. As a first attempt, the  $K_{IC(irr)}$  correlation was therefore developed to within a range of maximum damage of 5 dpa and a maximum irradiation temperature of 560 °C. Corresponding fracture toughness data for F82H in this damage and irradiation regime was used. Fig. 8 shows the fracture toughness for un-irradiated and irradiated F82H at a damage of 5 dpa irradiated at 300 °C, and Fig. 9 shows irradiated fracture toughness at a damage of 3.8 dpa irradiated between 221 °C and 405 °C. These data sets provide five  $K_{IC(irr)}$  data sets at irradiation temperatures, 220–280 °C (average 250 °C), 300 °C, 350–400 °C (average 375 °C), 380 °C, and 500 °C. In addition, one set of data at a constant irradiation temperature of 500 °C at two damage doses of 5 and 20 dpa is available. For the purpose of fitting the data, the values for  $K_{max}$  and  $K_0$  (upper/lower  $K_{IC}$ ) were taken to be the maximum and minimum reported value. The same holds for USE and LSE (Fig. 6).

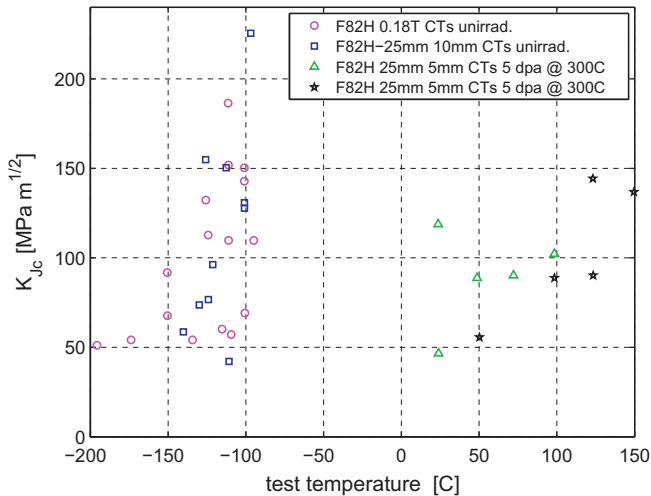


Fig. 8. Dependence of the fracture toughness,  $K_{IC}$  on temperature for F82H, before and after irradiation to 5 dpa [21].

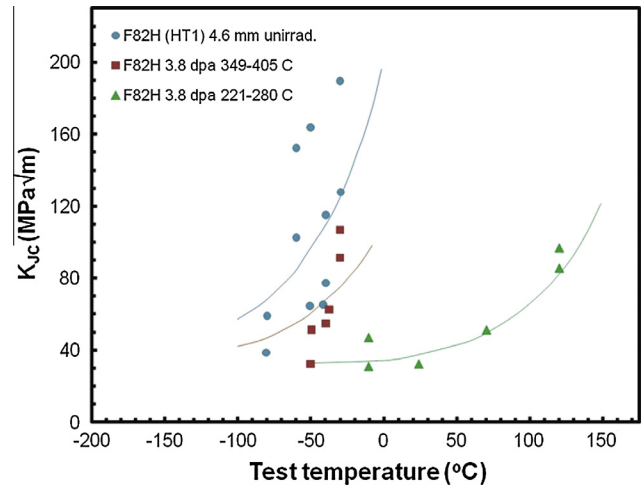


Fig. 9. Fracture toughness data for F82H as normalized and tempered and after irradiation in HFIR at 221–280 and 349–405 °C to approximately 3.8 dpa (note: all data for F82H (HT1) T-L 4.6 mm thick DC (T)[22]).

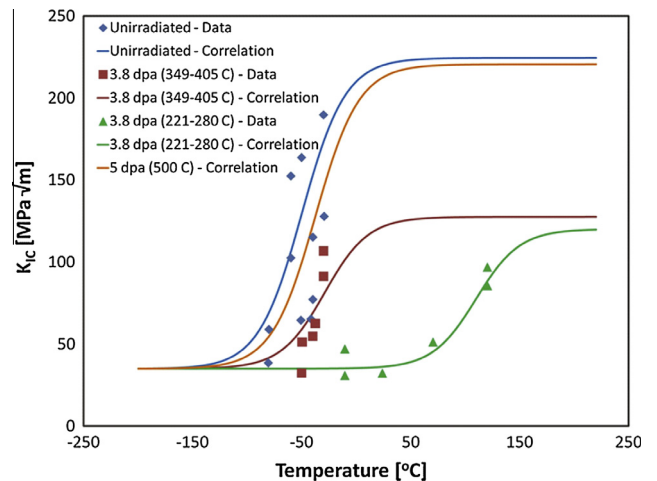


Fig. 10.  $K_{IC(irr)}$  correlation (Eq. (26)) fitted to experimental conditions [22].



The parameters  $A(T_{irr})$  and  $B(T_{irr})$  were derived from  $K_{IC(irr)}$  data for F82H at 3.8 dpa. In effect, acquiring the  $A$  and  $B$  parameters at a given dose effectively changes the  $K_{IC(irr)}$  correlation (Eq. (22)) to be a function of irradiation temperature only. This correlation will be useful for determining  $K_{IC(irr)}$  as a function of irradiation temperature at a given maximum dosage, such as in the case of the ITER TBM (maximum dose is 3.7 dpa). This approach was necessary, because the irradiated database for  $K_{IC(irr)}$  data of F82H is not large enough for establishing a  $K_{IC(irr)}$  correlation that is both damage and irradiation temperature dependent. A representative sample of the developed correlation for  $K_{IC}$  along with some of the experimental data is shown in Fig. 10.

#### 4. Conclusions

The current investigation is focused on providing a broad understanding of the key deformation mechanisms of F/M steels, their utilization in mechanical design and the inter-relationships between mechanical design and the structural properties of F/M steels. Several generations of steels have been developed both for the power industry (including fission systems), and for the more specialized applications in fusion energy systems. The impact of material property correlations and the mechanical design rules, outlined here, on the process of mechanical design is detailed in separate publications, for example, in references [27,28]. The present study points out to the following conclusions:

1. The optimization of steel composition is specific to its particular application. Most of the existing optimizations have been driven by the necessity for long-term service in power plant piping systems, and are not necessarily optimized for performance inside the core of fission reactors or in the first wall/blanket of fusion reactors. For such applications, optimization must be based on careful considerations of neutron activation (in the fusion case), irradiation effects on the mechanical properties, and life-limiting phenomena, in particular the interaction between creep and fatigue during transient operations.
2. Composition and processing optimization of steels is a compromise between mechanical design requirements and improvements of life-limiting properties. Presently, there seems to be little connection between these two aspects as far as steel optimization is concerned.
3. The requirements of mechanical design must therefore be considered at an early stage of material data base development and alloy optimization.
4. Although the available database for environmental and radiation effects can be cast in phenomenological or empirical forms, it is by no means certain that this process can be reliable for projection to unknown experimental regimes. This is particularly true for fusion energy applications, where the lack of 14 MeV neutron data implies large uncertainties in property extrapolations.
5. Modeling and simulation can be utilized to some extent in bridging this gap, with appropriate measures of uncertainty on the resulting property extrapolations.
6. Mechanical designs can often get around property limitations through adjustments in the configurations, boundary conditions or loading. It is thus imperative to couple mechanical design constraints with material property limitations in an

integrated fashion. This will allow directing attention to critical development path properties, and will make data generation, empirical extrapolation, and modeling efforts all the more useful and relevant.

#### Acknowledgments

This work is supported by the U.S. Department of Energy, Office of Fusion Energy Sciences through Grant # DE-FG02-03ER54708 with UCLA. The authors would like to acknowledge the contribution of Silvester Noronha, AREVA NP Inc., in collecting data on the DBTT. The critical editorial comments, and those of manuscript reviewers are greatly appreciated.

#### References

- [1] R.L. Klueh, *Int. Mater. Rev.* 50 (5) (2005) 287.
- [2] R. Klueh, D. Gelles, S. Jitsukawa, A. Kimura, G. Odette, B.V. der Schaaf, M. Victoria, *J. Nucl. Mater.* 307 (2002) 455–465.
- [3] N.M. Ghoniem, A. Shabaik, M.Z. Youssef, in: J.W. Davis, D.J. Michel (Eds.), *Proceedings of the Topical Conference on Ferritic Steels for Use in Nuclear Energy Technologies*, The Metallurgical Society of AIME, Warrendale, PA, 1984, pp. 201–208.
- [4] D.S. Gelles, N.M. Ghoniem, R.W. Powell, U.S. Patent Number 4,622,067, November 11, 1986.
- [5] M.K. Miller\*, D.T. Hoelzer, E.A. Kenik, K.F. Russell, *Intermetallics* 13 (2005) 387392.
- [6] A. Certain, T. Allen, D. Hoelzer, C. Parish, V. Shutthanandan, S. Kuchibhatla, *Study of Nanocluster Stability Nanostructured Ferritic Alloys (NFAs) Under High Dose Irradiation* ATR User Meeting, University of Wisconsin, Madison, WI, 2011.
- [7] M. Ashby, *Acta Metall.* 20 (1972) 887.
- [8] Harold J. Frost, M.F. Ashby, *Deformation-Mechanism Maps: The Plasticity and Creep of Metals and Ceramics*, Pergamon Press, 1982.
- [9] S. Zinkle, G. Lucas, *Fusion Materials Semiann, Progress Report* 20(DOE/ER-0313/34), 2003, pp. 101–125.
- [10] Meimei Li, Steven J. Zinkle, *J. Nucl. Mater.* 361 (2007) 192–205.
- [11] K. Shiba, N. Yamanouchi, A. Tohyama, *Fusion Mater. Semi-Ann. Progress Rep.* 20 (1996) 190–194.
- [12] A.K. Mukherjee, J.E. Bird, *J.D. Trans. Am. Soc. Metals* 62 (1969) 155.
- [13] T.E. McGreevy, *ANS Trans.* 94 (2006) 813–814.
- [14] V.N. Shah, S. Majumdar, K. Natesan, in: *Proceedings of the 4th International Symposium on Fusion Nuclear Technology (ISFNT-4)* NUREG/CR-6816, ANL-02/36, 2003.
- [15] ITER IDoMS S74MA1 97-12-12 RO.2Appendix A IDoMS G74MA2 98-06-26 FI, 1998.
- [16] S. Majumdar, P. Smith, in: *Proceedings of the 4th International Symposium on Fusion Nuclear Technology (ISFNT-4)*, 6–11 1997.
- [17] A.-A. Tavassoli, J. Rensman, M. Schirra, K. Shiba, *Fusion Eng. Des.* (2002) 617–628.
- [18] K. Shiba, A. Hishinuma, A. Kohyama, K. Matsamura, *Japan Atomic Energy Research Institute Report JAERI Tech97-038*, 1997.
- [19] Y. Dai, B. Long, Z. Tong, *J. Nucl. Mater.* 377 (2008) 115–121.
- [20] M. Ando, H. Tanigawa, E. Wakai, R. Stoller, *J. Nucl. Mater.* (2009) 315–318.
- [21] S. Jitsukawa, A. Kimura, A. Kohyama, R.L. Klueh, A.A. Tavassoli, B. van der Schaaf, G.R. Odette, J.W. Rensman, M. Victoria, C. Petersen, *J. Nucl. Mater.* (2004) 39–333.
- [22] R. Klueh, D. Gelles, S. Jitsukawa, A. Kimura, G.R. Odette, B.V. der Schaaf, M. Victoria, *J. Nucl. Mater.* (2002) 455–465.
- [23] H. Tanigawa, M. Sokolov, K. Shiba, R. Klueh, *Fus. Mater. Semi-Ann. Progress Rep.* 33 (2002) 66–72.
- [24] T. Yamamoto, G.R. Odette, H. Kishimoto, J. Rensman, P. Miao, *J. Nucl. Mater.* 356 (2006) 2749.
- [25] A. Moslang, in: *12th International Conference on Modern Materials and Technologies*, Montecatini, Italy, 2010.
- [26] B. van der Schaaf, C. Petersen, Y.D. Carlan, J. Rensman, E. Gaganidze, X. Averty, *J. Nucl. Mater.* (2009) 236–240.
- [27] S. Sharafat, A.T. Aoyama, N. Ghoniem, *Fus. Sci. Technol.* 60 (1) (2011) 264–271.
- [28] A.T. Aoyama, S. Sharafat, N. Ghoniem, M. Dagher, C. Wong, *Fus. Sci. Technol.* 60 (1) (2011) 170–174.